

Ferromagnetic Resonance in a Magnetically Dilute Percolating Ferromagnet: An Experimental and Theoretical Study

Y.K. Edathumkandy ¹ K. Das K. Gas ^{1, 2} D. Sztenkiel ¹
D. Hommel ^{3, 4} H. Przybylińska ¹ and M. Sawicki ^{1, 5}

¹*Institute of Physics, Polish Academy of Sciences,
Aleja Lotników 32/46, PL-02668 Warsaw, Poland*

²*Center for Science and Innovation in Spintronics, Tohoku University, Sendai 980-8577, Japan*

³*Lukasiewicz Research Network - PORT Polish Center for Technology Development, Stabłowicka 147, Wrocław 54-066, Poland*

⁴*Institute of Low Temperature and Structure Research,
Polish Academy of Sciences, Okólna 2, Wrocław 50-422, Poland*

⁵*Research Institute of Electrical Communication, Tohoku University,
Katahira 2-1-1, Aoba-ku, Sendai 980-8577, Japan*

Ferromagnetic resonance (FMR) serves as a powerful probe of magnetization dynamics and anisotropy in percolating ferromagnets, where short-range interactions govern long-range magnetic order. We apply this approach to $\text{Ga}_{1-x}\text{Mn}_x\text{N}$ ($x \simeq 8\%$), a dilute ferromagnetic semiconductor, combining FMR and superconducting quantum interference device magnetometry. Our results confirm the percolative nature of ferromagnetism in $(\text{Ga},\text{Mn})\text{N}$, with a Curie temperature $T_C = 12$ K, and reveal that despite magnetic dilution, key features of conventional ferromagnets are retained. FMR measurements establish a robust uniaxial anisotropy, dictated by Mn^{3+} single-ion anisotropy, with an easy-plane character at low Mn content. While excessive line broadening suppresses FMR signals below 9 K, they persist up to 70 K, indicating the presence of non-percolating ferromagnetic clusters well above T_C . The temperature dependence of the FMR intensity follows that of the magnetization, underscoring the stability of these clusters. Analysis of the FMR linewidth provides insights into relaxation processes, revealing large Gilbert damping due to the low magnetization of the system. Strikingly, atomistic spin model simulations reproduce the experimentally observed resonance fields, anisotropy trends, and linewidth evolution with remarkable accuracy. This agreement underscores the predictive power of our modeling approach in describing percolating ferromagnets. This study advances the understanding of percolating ferromagnetic systems, demonstrating that FMR is a key technique for probing their unique dynamic and anisotropic properties. Our findings contribute to the broader exploration of dilute ferromagnets and provide new insights into percolating ferromagnetic systems, which will be relevant for spintronic opportunities.

I. INTRODUCTION

The application of direct spin control in optoelectronic devices would be a large technological step forward. In this context dilute ferromagnetic semiconductors (DFS) have emerged as a subject of substantial research interest, due to their ability to blend the functionalities of semiconductors\insulators and the spin degrees of freedom [1, 2], thus paving the way to technological applications [3]. Within the systems being considered [4], $(\text{Ga},\text{Mn})\text{N}$ or $\text{Ga}_{1-x}\text{Mn}_x\text{N}$, with x representing the fraction of manganese ions distributed randomly on gallium sites, has gained substantial interest. This is mainly due to the high thermal stability of the wide band gap GaN host, that makes it suitable for use in extreme environments, such as outer space or harsh industrial settings.

Despite numerous attempts [5] the room temperature ferromagnetism (FM) of DFS remains an elusive goal of

materials science. In the case of Mn doped GaN the main reason is the insulating character of both $\text{GaN}: \text{Mn}$ [6] and $(\text{Ga},\text{Mn})\text{N}$ mixed crystals [7–9], which precludes magnetic coupling via itinerant carriers. In the wurtzite GaN lattice Mn is tetrahedrally coordinated by 4 neighboring nitrogen ions. In the absence of other intentional doping or charged point defects Mn assumes a neutral acceptor oxidation state, Mn^{3+} (d^4 configuration) [10, 11], for which the effective coupling mechanism is short-range *ferromagnetic* superexchange [7, 12, 13], confirmed for up to at least 25 near neighbors [14].

It is this superexchange coupling which induces the FM phase in $(\text{Ga},\text{Mn})\text{N}$, though its short range character and rather low Mn concentrations (not exceeding $x = 12\%$ [15] and typically below 10%) results in a percolating character of the ferromagnetism [16–18] realized in $(\text{Ga},\text{Mn})\text{N}$ only at the low end of cryogenic temperatures [13, 19–22]. This situation is very different from that of

the canonical DFS (Ga,Mn)As [23, 24], for which a robust global FM state can be stabilized up to above 170 K [25] by the hole-mediated long-range coupling for the same range of Mn compositions [2].

There are a few profound implications of the percolating form of FM in (Ga,Mn)N to our study. Whereas all of the spins are expected to be coupled at $T = 0$, only a fraction of the spins present in the material supports the FM state at nonzero temperatures. Starting from high temperatures, Mn spins form clusters of various shape and sizes and the Curie temperature T_C , marks that temperature at which the first infinite, percolating ("wall-to-wall") FM cluster forms. Therefore, at nonzero temperatures such a magnetic system is expected to behave as an ensemble of infinite and finite FM clusters (macrospins), characterized by a wide range of blocking temperatures and relaxation times.

This makes the magnetism, in general, and T_C , in particular, to depend on the characteristic measurement time (t_m) of the experimental technique in use. Similar to the blocking behavior in magnetically granular systems, the longer the t_m , the lower the characteristic temperature (in this case T_C), as more macrospins are given sufficient amount of time to reach equilibrium, in which they average out their contributions to the measured magnetic properties (e.g. magnetic moment m in case of magnetometry). Interestingly, this phenomenon is also observed in (Ga,Mn)As, where, due to various technological factors [26, 27] or deliberate measurement design [28–30], the material can be pushed toward the localization limit of holes. At this boundary, magnetic coupling is maintained only on mesoscopic scales [28, 31–33].

Another important factor is that Mn ions in GaN retain their single-ion magnetic anisotropy (SIMA), which is only weakly modified by their mutual FM coupling. Mn³⁺ ions in GaN adopt a high-spin configuration ($S = 2$, $L = 2$), with the ⁵T₂ state being the ground state. In the paramagnetic regime, a strong uniaxial magnetic anisotropy (UMA) emerges at low temperatures, differentiating the magnetic response depending on whether the external magnetic field \mathbf{H} is applied parallel or perpendicular to the hexagonal c -axis of the GaN crystal, i.e., $\mathbf{H} \parallel \mathbf{c}$ or $\mathbf{H} \perp \mathbf{c}$, respectively. This anisotropy arises from the trigonal distortion inherent to the wurtzite GaN lattice structure.

In the ideal tetrahedral coordination the ratio of the hexagonal lattice parameters $c/a = \sqrt{8/3}$. In pure GaN and at low Mn concentrations, $c/a < \sqrt{8/3}$, resulting in UMA with an easy-plane character, favoring spin alignment within the basal plane and making the c -axis the hard axis. However, upon increasing Mn concentration,

the situation changes significantly. For Mn content, x_{Mn} , exceeding about 10%, a transition to an elongated tetrahedron is anticipated in (Ga,Mn)N [20], which leads to a tensile trigonal distortion capable of reversing the easy magnetization direction to the c -axis.

Between these two regimes, an intriguing scenario may arise where the trigonal distortion is marginal, effectively nullifying UMA. Under such conditions, a significantly weaker threefold magnetic anisotropy could be potentially observed, originating from the static Jahn-Teller (JT) effect. This effect displaces N ions surrounding Mn ion, thereby lowering the local site symmetry of the Mn ion [34, 35]. Although the JT-related anisotropy is relatively weak, it plays a pivotal role in magnetization switching processes in FM (Ga,Mn)N [36].

To quantify the magnetic properties of paramagnetic Mn³⁺ in GaN one can use the crystal-field model (CFM) [37–39] developed originally for Cr²⁺ in II-VI semiconductors [40–42] and adopted to Mn³⁺ in GaN [34, 36, 38, 43–45]. However, this exact quantum-mechanical approach to the magnetism of Mn in GaN becomes computationally challenging, as the Hamiltonian matrix size grows exponentially with the number of interacting neighboring Mn ions considered. To overcome this limitation, a classical approximation - an atomistic spin model [46] - has been successfully applied to (Ga,Mn)N. In this framework, employed also in this study, the stochastic Landau–Lifshitz–Gilbert (sLLG) method is used to describe the precessional dynamics of spins, represented as classical vectors [36, 47].

Prior studies have definitively shown the importance of investigating static micro-magnetic properties in (Ga,Mn)N layers [7, 13, 21, 43]. The manipulation of magnetic anisotropy in (Ga,Mn)N using electric fields was successfully demonstrated in both the paramagnetic [44] and FM case [36]. Furthermore, using the spin Hall magnetoresistance technique [48], the spectrum of (Ga,Mn)N functionalities was recently supplemented by the demonstration of efficient generation and detection of spin currents in Pt/(Ga,Mn)N structures up to 50 K [49], i.e., well above the Curie temperature established upon magnetometry method. Despite these advancements, our understanding of the dynamics and relaxation processes of magnetization within (Ga,Mn)N, along with the intricate physics governing magnetic anisotropy, remains in its infancy. To address these shortcomings, the ferromagnetic resonance (FMR) technique is employed, a highly precise method renowned for its capability to probe the dynamic magnetic properties of ferromagnetic thin films [50].

FMR is the ideal method for comprehensively assessing

fundamental characteristics, including absolute values of magnetic anisotropies, Curie temperature, magnetoelastic coupling coefficients, and parameters describing magnetization relaxation [51]. While FMR techniques have been instrumental in exploring the dynamics and relaxation processes of magnetization in other DFS [51–54], the realm of (Ga,Mn)N remains largely uninvestigated in this context. This is primarily due to the fact that, unlike Mn²⁺ (d^5 configuration), the paramagnetic Mn³⁺ ion in GaN tetrahedral coordination is EPR silent in typical X-band spectrometers. Consequently much of the information available today on the properties of the Mn³⁺ state in GaN was established by optical spectroscopy [38, 39] and low-temperature and high-field magnetometry [34, 38, 43, 55]. In this context, the robust FM state observed in (Ga,Mn)N [21] allows us to address the material using classical EPR equipment by studying FMR, the collective response of the otherwise EPR-silent Mn³⁺ ions. Our study, therefore, aims to expand the pool of understanding of this dilute magnetic percolating system well beyond the limits of static SQUID measurements (t_m of the order of seconds) into the realm of GHz, specific to FMR technique.

In this work, we concentrate on a thorough investigation of magnetic properties of the insulating ferromagnetic $\text{Ga}_{1-x}\text{Mn}_x\text{N}$ layer with an Mn concentration of $x = 7.9\%$ by applying the FMR technique and superconducting quantum interference device (SQUID) magnetometry. Our primary focus lies in analyzing the temperature dependence of the resonance field and its correlation with the angular orientation of the applied magnetic field. This approach allows us to determine critical parameters such as the Curie temperature, the effective g -factor, and magnetic anisotropy constants across varying temperatures. Moreover, our investigation extends to explore the temperature and angular-dependent line width of the signal. This analysis is crucial in unveiling valuable insights into material inhomogeneities and relaxation mechanisms in (Ga,Mn)N.

II. METHODS

A. Experiment

1. Samples

(Ga,Mn)N layers with various thicknesses up to about $1 \mu\text{m}$ are grown by the molecular beam epitaxy (MBE) technique on fully relaxed GaN templates (about $2\mu\text{m}$ thick) deposited by MOVPE on *c*-plane 0.3 - 0.4 mm thick Al₂O₃ substrates, following the specifications elaborated previously to obtain single phase epitaxial lay-

ers without traceable amounts of other magnetic phases [20, 22]. The surface quality of the layers was monitored *in situ* during growth using reflection high-energy electron diffraction. High quality and single phase of the material are confirmed by high-resolution X-ray diffraction.

2. Experimental procedures

Magnetic measurements are performed in a Quantum Design superconducting quantum interference device (SQUID) MPMS-XL magnetometer with a low field option to measure magnetic properties at magnetic fields up to 70 kOe and temperatures between 2 and 400 K. Strict protocols are followed to avoid artifacts and limitations of volume SQUID magnetometry of thin films deposited on bulky substrates [56–58]. Measurements of a bare GaN template substrate serve as a reference signal to eliminate the interference of disturbing low-temperature magnetic anisotropy of commercial sapphire substrates [59]. The remaining relevant details are given in Appendix A.

Ferromagnetic resonance experiments are conducted with use of a BRUKER EMX plus spectrometer operating at 9.5 GHz ($h\nu = 39 \mu\text{eV}$) and equipped with an Oxford Instruments 910 Cryostat enabling temperature control from 3 to 300 K and 360 deg sample rotation with respect to the static external magnetic field \mathbf{H} . The recorded FMR signal is the magnetic field derivative of the absorbed microwave power that is proportional to the imaginary part of the AC magnetic susceptibility χ'' .

B. Numerical simulations

The experimental data are modeled using an atomistic spin model [46] combined with the stochastic Landau-Lifshitz-Gilbert (sLLG) equation [36, 47]. Simulations are performed on a system consisting of 9860 randomly distributed Mn spins in a wurtzite lattice, with in-plane periodic boundary conditions to model a large thin film. The classical spin Hamiltonian accounts for Zeeman energy, magnetocrystalline anisotropy, and ferromagnetic superexchange interactions between Mn ions taken exactly up to the 14th coordination sphere [18]. The spin dynamics are governed by the sLLG equation, and the magnetization and FMR response are computed as a function of external magnetic field and temperature. A Monte Carlo method is employed to simulate thermo-remanent magnetization. [60, 61].

Of particular importance in this study is an attempt to model FMR measurements. To this end the simulation

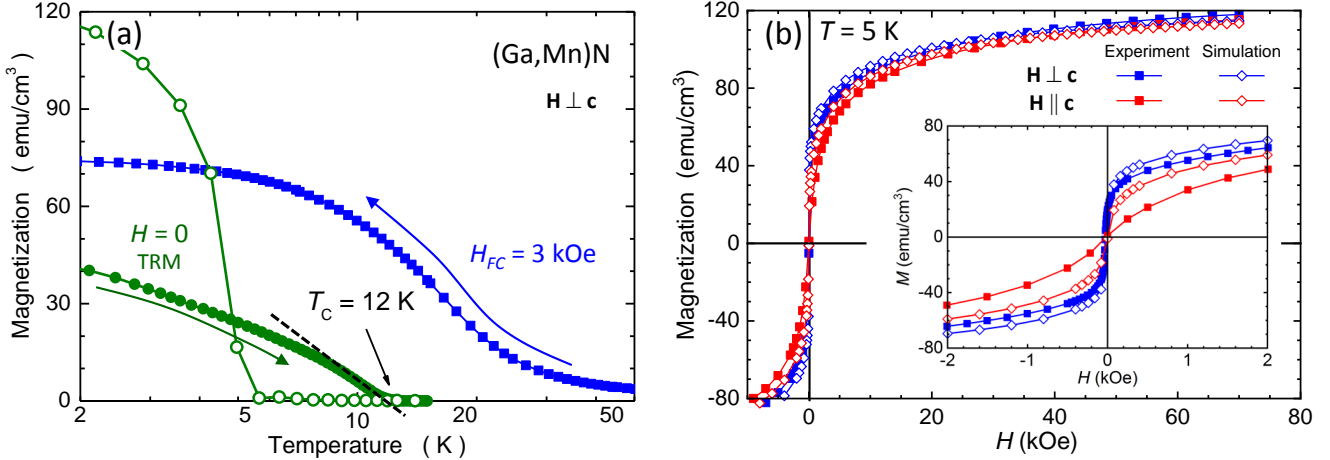


Figure 1. (Color online) Comparison of experimental (solid symbols) and simulated with the atomistic spin model (open symbols) magnetization curves for $(\text{Ga},\text{Mn})\text{N}$ film with $x_{\text{Mn}} = 7.9\%$. (a) Temperature dependence of the thermo-remnant magnetization (TRM) for the in-plane orientation of H (green circles). The initial field-cooled (FC) magnetization measured during cooling at $H_{\text{FC}} = 3 \text{ kOe}$ is shown as solid blue squares. The temperature at which TRM vanishes defines the Curie temperature, T_C , of the film. Open circles represent results from atomistic spin model and Monte Carlo simulations. (b) Magnetization as a function of magnetic field, H , measured at $T = 5 \text{ K}$ for two field orientations: perpendicular to the c -axis (blue) and along the c -axis (red). The inset provides an expanded view of the low-field region near $H = 0$.

box is numerically subjected to an AC magnetic field [62], and the resonance field and line-width are extracted from the simulation results. Details of the simulation methodology, including the full Hamiltonian, equations of motion, and parameter values, are provided in Appendix B.

III. RESULTS AND DISCUSSIONS

A. Magnetic characterization

The Curie temperature, T_C , is the main parameter describing any ferromagnetic material [63], yet its determination has remained a challenge despite numerous advances in this field. The challenge grows in magnetically dilute materials when the critical features become smeared over a wide temperature range. In this study, we employ the thermoremanent magnetization (TRM) measurements as the least cumbersome method of the determination of T_C in DFS, regardless of the range of the FM interaction [21, 22, 64, 65].

To acquire TRM data the sample is initially field-cooled in a magnetic field of $H_{\text{FC}} = 3 \text{ kOe}$ [blue squares in Fig. 1 (a)]. After quenching the field at $T = 2 \text{ K}$ the TRM is recorded during warming [green bullets in Fig. 1 (a)]. The temperature at which TRM vanishes indicates the $T_C = 12 \text{ K}$ in this film. More in-depth experimental considerations pertinent to this technique are outlined in Appendix A.

Exemplary magnetization curves, $M(H)$, obtained for the same sample at $T = 5 \text{ K} < T_C$ are shown in Fig. 1 (b) as solid symbols. Despite being in the FM state, the sample exhibits a considerable rounded $M(H)$ dependence at low magnetic fields [19–22, 36, 45, 66]. This behavior arises directly from the significant magnetic dilution and short-range character of the superexchange interaction, both giving rise to the percolative nature of the FM coupling.

On a microscopic level, this effect manifests itself as a broad distribution of ferromagnetically coupled clusters of varying sizes, meaning that at weak magnetic fields, hysteresis involves only a fraction of the spins. At this level of dilution, $(\text{Ga},\text{Mn})\text{N}$ does not form a uniform ferromagnetic phase below T_C . Moreover, the $M(H)$ data indicate that magnetization does not fully saturate even at fields as high as 70 kOe. This behavior arises from the significant contribution of the weakly saturating orbital moment to the total magnetic moment of Mn^{3+} ions [67].

The results of the simulations of the corresponding magnetizations, $\text{TRM}(T)$ in Fig. 1 (a) and $M(H)$ in Fig. 1 (b), are represented by open symbols. Given the relatively simplified assumptions underlying our computational approach, this level of agreement can be considered as a significant achievement. Notably, the calculated Curie temperature differs from the experimentally determined value by only a factor of two.

A particularly good correspondence is observed for the

$M(H)$ dependence, especially at high magnetic fields. The main quantitative discrepancies arise near $H = 0$, as highlighted in the inset of Fig. 1 (b), and in the simulation of TRM(T). In general, the simulations tend to overestimate M in the low-field regime. This discrepancy likely stems from the limitations of our current model, which does not fully account for the complexity of the real Mn distribution in (Ga,Mn)N. The primary simplification lies in the assumption of an ideal wurtzite GaN environment surrounding each Mn ion, where the magnetic response is treated within the single-ion anisotropy approach. While the model includes spin-spin interactions, it assumes that each Mn ion remains embedded in a locally undisturbed crystalline field. As a result, the computation scheme does not incorporate local symmetry breaking induced by neighboring Mn³⁺ ions [35]. This effect modifies the anisotropy landscape and becomes particularly relevant at low fields, where the Zeeman energy is small.

B. Temperature dependence of the FMR

Fig. 2 (a) depicts the temperature dependence of the ferromagnetic resonance spectra when \mathbf{H} is applied along the out-of-plane direction ($\mathbf{H} \parallel [0001]$). The hard direction was chosen to minimize the effects of superposition of the FMR signal with the cyclotron resonance (CR) background signal stemming from the conducting GaN template. In contrast to SQUID results, at low temperatures (up to 7 K) only a strong CR and a very weak defect-related paramagnetic signal at $g = 2$ are visible. Ferromagnetic signatures start to appear around $T = 9$ K and their integrated intensity gradually decreases with increasing temperature to disappear entirely above $T = 70$ K. The lack of FMR signals below $T = 9$ K is due to the very fast relaxation rate of the magnetization which makes the FMR signal too broad to be detected. This will be discussed in detail in Section III D.

In order to compare the FMR results with the magnetization measured with SQUID at nonzero magnetic fields we fit the signals with the derivative of a Lorentzian function:

$$A \frac{d}{dH} \left[\frac{\Delta H}{(H - H_R)^2 + \Delta H^2} + \frac{\Delta H}{(H + H_R)^2 + \Delta H^2} \right], \quad (1)$$

to establish the amplitude A , H_R , and the half width at half maximum (HWHM) ΔH at each temperature. In the fits we also include the influence of the substrate free electron absorption, which at high enough fields can be approximated by the sum of a decreasing exponential function and a linear increase with H . The fits are denoted by black dashed lines in Fig. 2 (a). The FMR intensity, I , is then calculated as $I = A \times \Delta H$ and

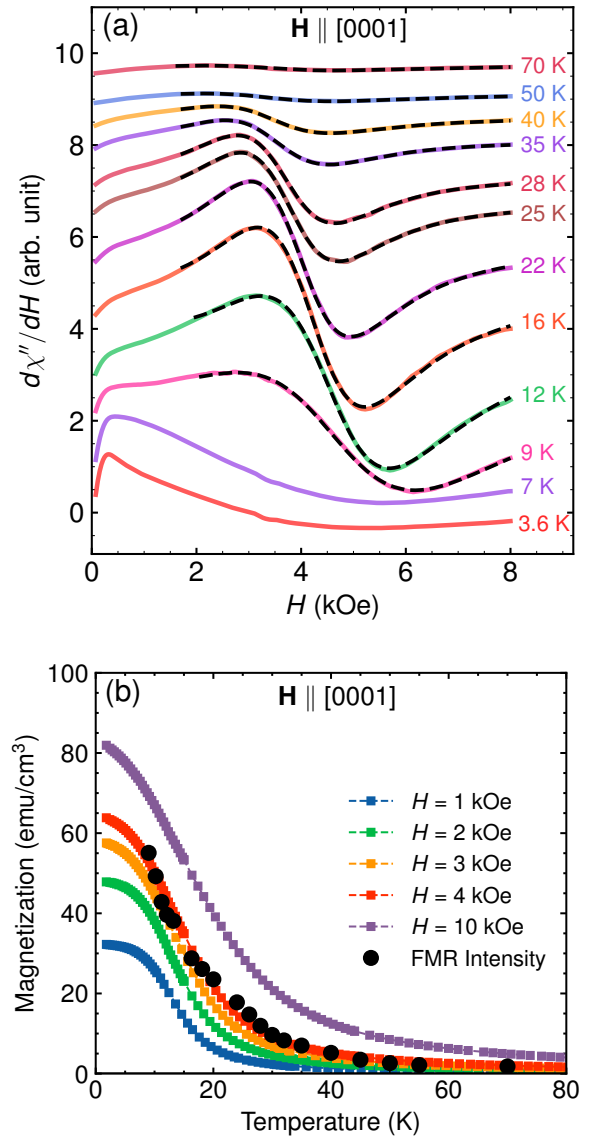


Figure 2. (a) Selected, temperature dependent ferromagnetic resonance spectra measured with magnetic field \mathbf{H} applied along the out-of-plane, $[0001]$ crystallographic axis of the (Ga,Mn)N film. The spectra are shifted vertically for clarity. Black dashed lines are fits of Eq. 1. (b) Temperature dependence of the ferromagnetic moment calculated by double integration of the FMR signals (black circles) compared to the magnetization of the (Ga,Mn)N film measured in the same configuration at a few magnetic fields H (indicated in the graph).

is directly proportional to the magnitude of the ferromagnetic moment. In the absence of magnetocrystalline anisotropy it would be possible to obtain absolute values of magnetization from the in- and out-of-plane FMR measurements. This is not the case here. Therefore, we adjust the established intensity of the FMR signal to the magnetization value determined from SQUID at 3

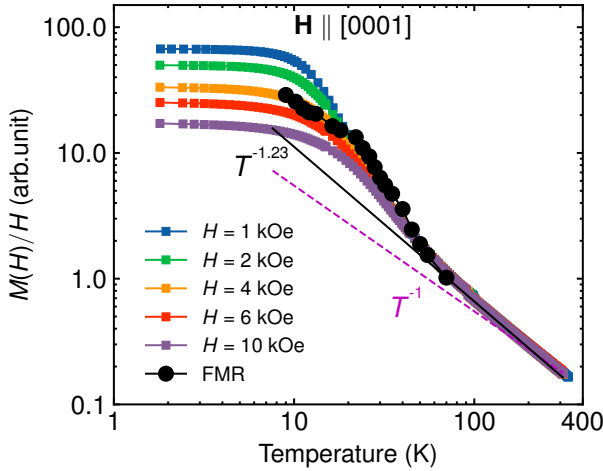


Figure 3. Temperature T dependence of the magnetic susceptibility, $\chi(T) = M(T)/H$, established for the $(\text{Ga},\text{Mn})\text{N}$ film between 1 and 10 kOe plotted in a double logarithmic scale (small symbols). Black circles show the temperature dependence of the FMR intensity divided by the resonance field I/H_R . The dashed gray line indicates the Curie law, i.e. the proportionality to $1/T$, whereas the solid black line indicates that $\chi(T) \propto T^{-1.23}$ at high temperatures, as expected for a random paramagnet with ferromagnetic excitations.

kOe and 55 K. As shown in Fig. 2 (b) a close correspondence is observed between the $M(T)$ values measured between $H = 3$ and 4 kOe and $I(T)$ (black circles) derived from the FMR data. In both cases the transition temperature exceeds T_C . The fact that the FMR signal persists up to $T = 70$ K is attributed to the magnetic field ($H = 3.3$ kOe) applied in the FMR experiment, which acts against thermal fluctuations [52, 68], and the presence of non-percolating ferromagnetic clusters above T_C .

To substantiate this scenario we re-draw the magnetometry and FMR results in a double logarithmic scale, Fig. 3, since in amorphous systems with a wide range of exchange integrals the $\chi(T) = M(T)/H$ above their specific coupling temperature is expected to be proportional to $T^{-\alpha}$ [69, 70]. Obviously, $\alpha = 1$ for non-interacting systems (the Curie law) and this dependency is marked by a dashed line in Fig. 3. However, the presence of interactions tends to form spin pairs and higher order complexes which reduce/enhance the magnetization with respect to T^{-1} for antiferromagnetic/ferromagnetic coupling among the spins. As a result $\alpha < 1$ for random antiferromagnets. Here Mn- or Co-based II-VI dilute magnetic semiconductors are good examples [71–73]. Analogously, $\alpha > 1$ for ferromagnetic coupling, and $(\text{Ga},\text{Mn})\text{N}$ is the prime example here [21]. Our magnetometry data plotted in Fig. 3 follow the same trend as in [21] yielding $\alpha = 1.23$ for

$T > 80$ K (marked by the solid black line). This behavior is obeyed at high temperatures independently of the magnitude of H , at least within 1 to 10 kOe range. However, below 70 K the whole group of curves deviates up from the $T^{-1.23}$ trend, and start to fan-out below 30 K, though not signalizing any critical behavior around T_C . The FMR results follow the same trend. In particular they align within $M(H)/H$ data obtained for $H = 3$ or 4 kOe. The former finding confirms that $I(T)$ proxies the $\chi(T)$ of $(\text{Ga},\text{Mn}^{3+})\text{N}$. This is only the case as long as the Mn^{3+} ions form sufficiently large ferromagnetically ordered clusters - macrospins - which absorb coherently the microwave energy.

The pertinent question arises about the size of these FM-coupled entities. The direct quantum-mechanical computations of $\text{Ga}_{0.97}\text{Mn}_{0.03}^{3+}\text{N}$ with nearest neighbors complexes taken into account up to the forth order (that is pairs, triplets and quartets) [45] showed only marginal improvement over the case of non-interacting Mn^{3+} singles. This proves that the FM-like macrospins puddles must contain $N \gg 4$ Mn ions.

C. Magnetocrystalline anisotropy

Ferromagnetic resonance is the easiest experimental technique to investigate magnetocrystalline anisotropy. For this purpose we have chosen to rotate the external magnetic field in the $(\bar{1}\bar{1}00)$ plane, which contains all the relevant crystallographic directions, including the $\langle 100 \rangle$ cubic axes along which static Jahn-Teller distortions occur [74]. However, the low temperature line broadening and the background cyclotron resonance of the GaN template precludes angular dependent investigations below 12 K. The experimental geometry is shown schematically in Fig. 4 (a). Selected FMR spectra recorded for different orientations of the applied magnetic field are presented in Fig. 4 (b), while the angular dependence of the determined resonance fields is given in Fig. 4 (c) (symbols). The solid line in Fig. 4 (c) is calculated with the use of the Smit-Beljers equation [75]:

$$\hbar\nu = \frac{g\mu_B}{M \sin \theta_{eq}} \sqrt{\frac{\partial^2 F}{\partial \theta^2} \frac{\partial^2 F}{\partial \varphi^2} - \left(\frac{\partial^2 F}{\partial \theta \partial \varphi} \right)^2} \Big|_{\theta_{eq}, \varphi_{eq}}, \quad (2)$$

where $\nu = 9.5$ GHz is the uniform mode resonance frequency, g is the effective spectroscopic splitting factor, μ_B is the Bohr magneton, θ and φ are the polar and azimuthal angles of the magnetization vector, \mathbf{M} , defined in Fig. 4 (a), and F is the anisotropic part of the magnetic free energy density. The equilibrium angles of \mathbf{M} ($\theta_{eq}, \varphi_{eq}$) are determined by minimizing F . In the coor-

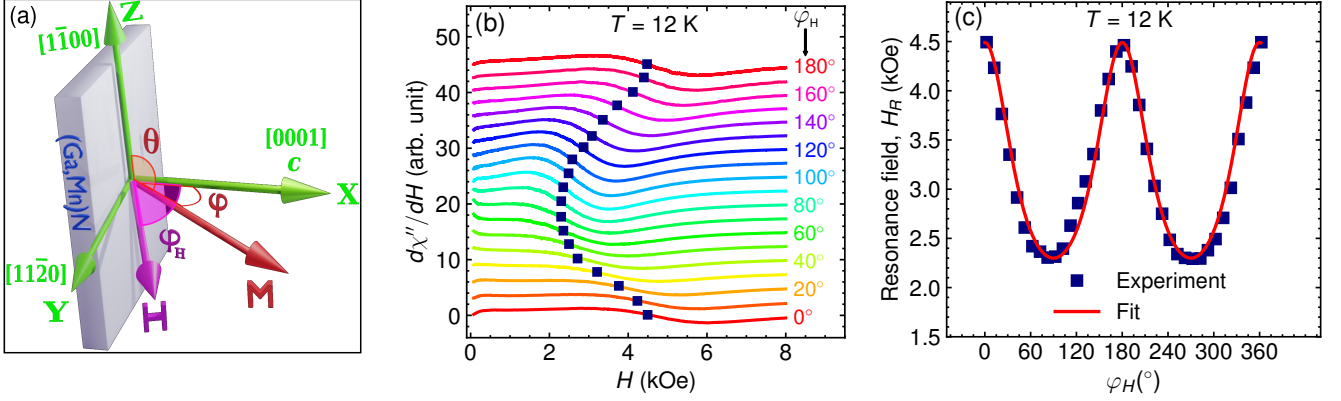


Figure 4. (Color online) (a) Scheme of the FMR measurements geometry emphasizing the coordinate system used. The applied dc magnetic field vector \mathbf{H} lies in the (1-100) plane and the azimuthal angle φ_H is counted from the [0001] (X) axis. The orientation of the magnetization vector \mathbf{M} is given by the azimuthal φ and polar θ angles, the latter counted from the [1-100] (Z) axis. In principle, \mathbf{H} and \mathbf{M} are not collinear. (b) Selected, angularly dependent ferromagnetic resonance spectra recorded with the magnetic field rotated in the (1-100) plane at $T = 12$ K. Symbols indicate resonance field values. (c) Angular dependence of the resonance fields H_R for the magnetic field \mathbf{H} rotated in the (1-100) plane at $T = 12$ K. Symbols represent experimental data, the solid line is a fit.

dinate system of Fig. 4 (a) F is given by:

$$F = -MH \sin \theta \cos(\varphi - \varphi_H) + (2\pi M^2 - K_2) \sin^2 \theta \cos^2 \varphi. \quad (3)$$

Here, the first term describes the Zeeman energy, whereas the second term is a combination of the thin film demagnetization energy ($2\pi M^2$) and the uniaxial magnetocrystalline anisotropy energy (K_2) along the [0001] axis. We adhere to the standard convention that the sign of the uniaxial anisotropy is opposite to that defined in the electron paramagnetic resonance Hamiltonian [50]. Higher order terms in F are omitted. Since $\frac{\partial F}{\partial \theta} = 0$ for $\theta_{eq} = 90^\circ$ the magnetization vector also lies in the (1-100) rotation plane. Defining an effective uniaxial anisotropy field H_2 as:

$$H_2 = 2\pi M - \frac{K_2}{M} \quad (4)$$

we obtain the following equations:

$$\left(\frac{h\nu}{g\mu_B} \right)^2 = \{ H_R \cos(\varphi - \varphi_H) - 2H_2 \cos^2 \varphi \} \times \{ H_R \cos(\varphi - \varphi_H) - 2H_2 \cos 2\varphi \}, \quad (5)$$

$$H_R \sin(\varphi - \varphi_H) = H_2 \sin 2\varphi, \quad (6)$$

which can be solved analytically. The relation between φ_H and φ is given by:

$$\varphi_H = \varphi - \arcsin \left(\frac{H_2 \sin 2\varphi}{H_R} \right). \quad (7)$$

The best fit of Eqs:(5)-(7) to the experimental data is shown by solid line in Fig. 4 (c). It yields $H_2 = 0.77$ kOe and $g = 2.29$. The uniaxial anisotropy energy density, determined by subtracting the magnetization value obtained from SQUID measurements at 4 kOe and $T = 12$ K, is $K_2 = -2.1 \times 10^4$ erg/cm³.

The temperature dependence of the uniaxial anisotropy is obtained from FMR signals at two orientations of the applied magnetic field: $\mathbf{H} \parallel [0001]$ ($\varphi_H = 0^\circ$) and $\mathbf{H} \parallel [11\bar{2}0]$ ($\varphi_H = 90^\circ$). The temperature dependences of H_R for these two field orientations are shown in Fig. 5 (a). With increasing temperature the resonance fields monotonically approach the value corresponding to $g = 2$, characteristic of non-interacting Mn³⁺ ions, as shown by the temperature dependence of the effective g -factor in the inset. This finding is consistent with the magnetic $M(H)/H$ vs. T data (Fig. 3), where deviations from the high-temperature trend $T^{-1.23}$ occur at approximately the same temperature at which g -factor starts to deviate from 2, indicating the onset of detectable ferromagnetic coupling among some Mn³⁺ ions.

The temperature dependence of the effective anisotropy fields H_2 determined from the data presented in Fig. 5 (a) is shown in Fig. 5 (b), together with that of demagnetization fields $2\pi M$ obtained from SQUID measurements at $H = 4$ kOe (Fig. 2 (b)). These two dependencies allow us to approximate the temperature behavior of the uniaxial magnetocrystalline energy density K_2 which is shown in Fig. 5 (d). As can be seen, K_2 is negative in accordance with the fact that the [0001] crystallographic

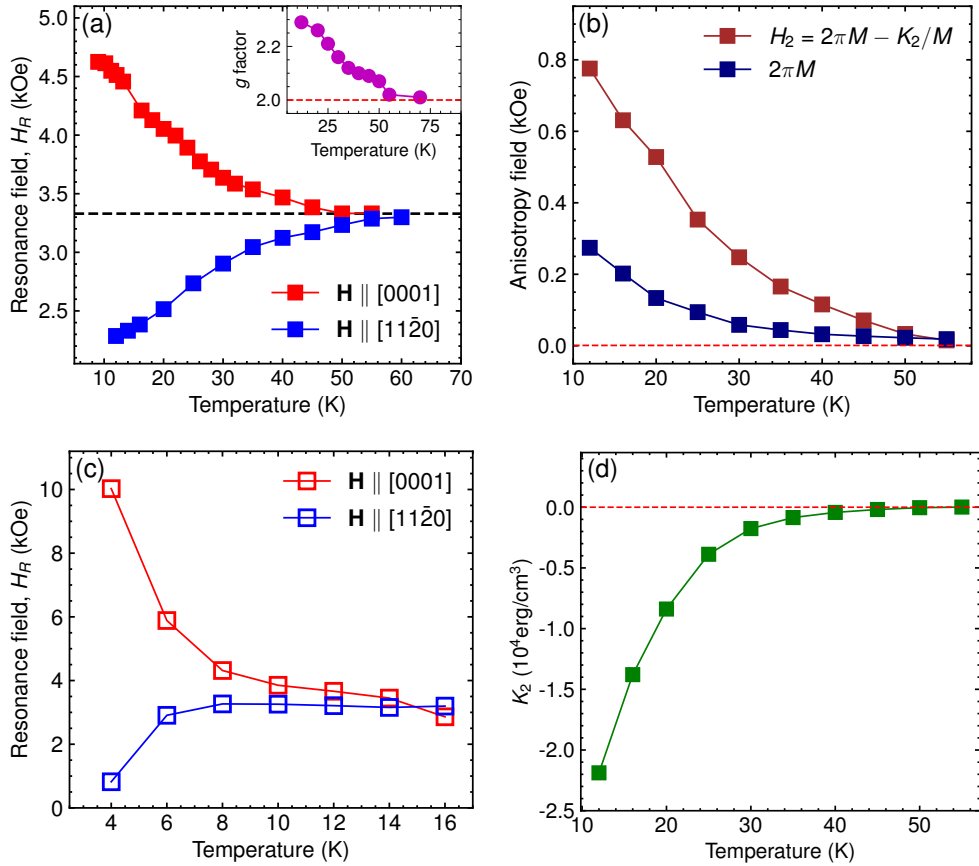


Figure 5. (Color online) (a) Temperature dependence of the resonance fields H_R for two magnetic field orientations: $\mathbf{H} \parallel [0001]$ (red symbols) and $\mathbf{H} \parallel [11\bar{2}0]$ (blue symbols). The dashed line marks the field corresponding to $g = 2$. The inset shows the temperature dependence of the effective g-factor. (b) Temperature dependence of the anisotropy field H_2 and the demagnetization field $2\pi M$ (brown and navy squares, respectively). The latter is determined using the magnetization data shown in the inset of Fig. 2 for $H = 4$ kOe. (c) Simulation results depicting the temperature dependence of H_R for two magnetic field orientations: $\mathbf{H} \parallel [0001]$ (open red symbols) and $\mathbf{H} \parallel [11\bar{2}0]$ (open blue symbols). (d) Temperature dependence of the uniaxial magnetocrystalline anisotropy energy K_2 , obtained from (b). The solid line is a guide for the eye.

axis (c axis) of GaN is the hard magnetization direction in $(\text{Ga,Mn})\text{N}$. With increasing temperature the absolute value of K_2 decreases monotonically to zero.

Figure 5 (c) illustrates the temperature dependence of the resonance field $H_R(T)$ obtained from numerical simulations. As in the experimental data, we analyze two configurations: \mathbf{H} applied along the out-of-plane [0001] direction and the in-plane [1120] direction. The simulation results qualitatively reproduce the experimental trends shown in Fig. 5 (c), albeit in about four times narrower temperature range. However, the same pronounced anisotropy in H_R is observed at low temperatures between the two directions, with the out-of-plane configuration exhibiting significantly larger resonance fields. This anisotropy gradually diminishes with increasing temperature, and H_R converges to approximately the same value as observed in the experiment, about 3.3 kOe.

The low value of the uniaxial anisotropy constant K_2 as compared to those reported for various ferromagnetic transition metals showing room temperature ferromagnetism (e.g. Ref.[50] and references therein) is easily explained bearing in mind the rather moderate magnetic moment resulting both from the low Mn concentration as well as the partial quenching of the spin-orbit interaction (which is the main source of anisotropy in non-metallic ferromagnets) by the Jahn-Teller effect [74]. As the 4-th order terms in the magnetic free energy density are usually an order of magnitude weaker than the uniaxial terms, the lack of such anisotropy terms in the experimental data is not unexpected.

Interestingly, no influence of the static Jahn-Teller distortion on the $H_R(\varphi)$ dependence is observed, contrary to expectations. Specifically, no broadening of the FMR signals is detected along the $\langle 100 \rangle$ cubic axes directions (detailed in the next Section). This result suggests a

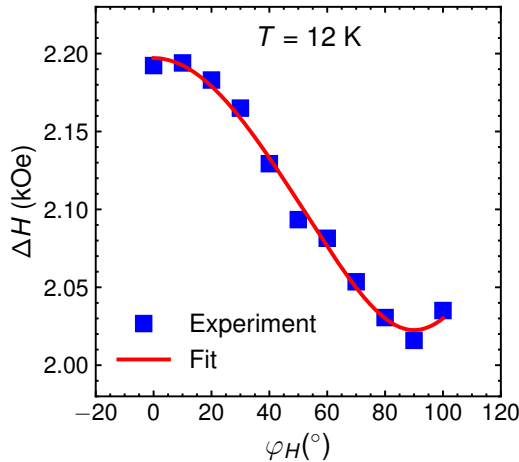


Figure 6. (Color online) Angular dependence of the linewidth ΔH measured at 12 K with the applied magnetic field \mathbf{H} rotated in the (1̄100) crystal plane (symbols). The line is a fit obtained with Eqs. (8) and (11) for $\Delta H_{homo} = 2.07$ kOe and $\Delta H_2 = 63$ Oe.

transition from a static Jahn-Teller effect, previously reported at 2 K [74], to a dynamic regime at $T \simeq 12$ K, where cubic distortion directions are averaged. This observation is intriguing and warrants further investigation.

D. FMR linewidth and relaxation in (Ga,Mn)N

The investigation of the FMR linewidth (ΔH) can give valuable information on the relaxation rate of the magnetization as well as potential inhomogeneities of the studied system. ΔH is expressed as:

$$\Delta H = \Delta H_{homo} + \Delta H_{inhomo} \quad (8)$$

Here, the first term represents the contribution to ΔH originating from the intrinsic damping of the magnetization precession, while the second term takes into account the contribution related to magnetic and/or structural inhomogeneities in the system. ΔH_{homo} is both frequency and angularly dependent and is given by [76]:

$$\Delta H_{homo}(\theta, \varphi) = \frac{G}{M^2} \left(\frac{\partial^2 F}{\partial \theta^2} + \frac{1}{\sin^2 \theta} \frac{\partial^2 F}{\partial \varphi^2} \right) \Bigg/ \left| \frac{\partial \omega}{\partial H_R} \right|, \quad (9)$$

where G is the Gilbert damping parameter. In the (1̄100) rotation plane it simplifies to [77]:

$$\Delta H_{homo}(\theta, \varphi) = \left(\frac{\hbar}{g\mu_B} \right)^2 \frac{G\omega}{M \cos(\varphi - \varphi_H)}. \quad (10)$$

One should, therefore, expect minimum linewidths only for two magnetic field directions, since $\varphi_H - \varphi = 0$

only for in-plane and out-of-plane orientations of \mathbf{H} . Instead, the angular dependence of the linewidth measured at 12 K and shown in Fig. 6 resembles that of H_R (Fig. 4 (c)), with maximum and minimum ΔH values at $\mathbf{H} \parallel [0001]$ and $\mathbf{H} \parallel [11\bar{2}0]$, respectively. Such a dependence is expected for inhomogeneous line broadening, arising from a distribution of magnetic moments and anisotropy fields within the sample, which can be expressed as [78]:

$$\Delta H_{inhomo} = \Delta H_2 \frac{\partial H_R}{\partial H_2}. \quad (11)$$

The fit of experimental data with Eqs.(8) and (11) presented by the solid line in Fig. 6 gives $\Delta H_{homo} = 2070$ Oe and $\Delta H_2 = 63$ Oe. In the fit the angular dependence of ΔH_{homo} is neglected. It is evident that the main contribution to the linewidth is due to intrinsic damping. The Gilbert parameter determined from ΔH_{homo} is about 4×10^8 s⁻¹ for \mathbf{H} along [0001] at 12 K and does not differ much from the values found for typical ferromagnetic metals [50]. The reason for the untypically broad linewidth is the low value of magnetization [$M \simeq 45$ emu/cm³, as indicated in Fig. 2 (b)], which enters in the denominator of Eq.(10). This explains also the unusually high value of the parameter $\alpha_G = \frac{\hbar G}{g\mu_B M} = 0.68$ as compared to typical values observed in diluted magnetic systems and metals [50, 79, 80].

The contribution of ΔH_{inhomo} to the total linewidth at 12 K is at most 6%, despite the large value of the anisotropy field ($H_2=0.77$ kOe). This results from the small $\Delta H_2/H_2$ ratio of 8.2%, which points to a rather homogeneous distribution of Mn ions in the sample.

Fig. 7 (a) illustrates the temperature dependence of ΔH measured for \mathbf{H} applied along the out-of-plane [0001] and in-plane [11̄20] directions. As shown, the linewidth narrows with increasing temperature in both configurations, reaching minimum values at approximately 26 K and 35 K, as marked in the figure. This narrowing is only partly due to decreasing anisotropy fields [shown in Fig. 5 (b)], but is mostly due to a reduction of the the Gilbert damping parameter G with increasing temperature. The temperature dependence of G extracted from the experimental data is presented in Fig. 7 (c) for in- and out-of-plane magnetic field directions. As can be seen, the damping parameter decreases monotonically with increasing temperature and is consistently greater for the magnetic field applied along the hard axis than for the in plane orientation. The anisotropy of G contributes to the observed difference in the temperature dependences of the in-plane and out-of-plane linewidths shown in Fig. 7 (a).

The sharp increase in linewidths above the minimum

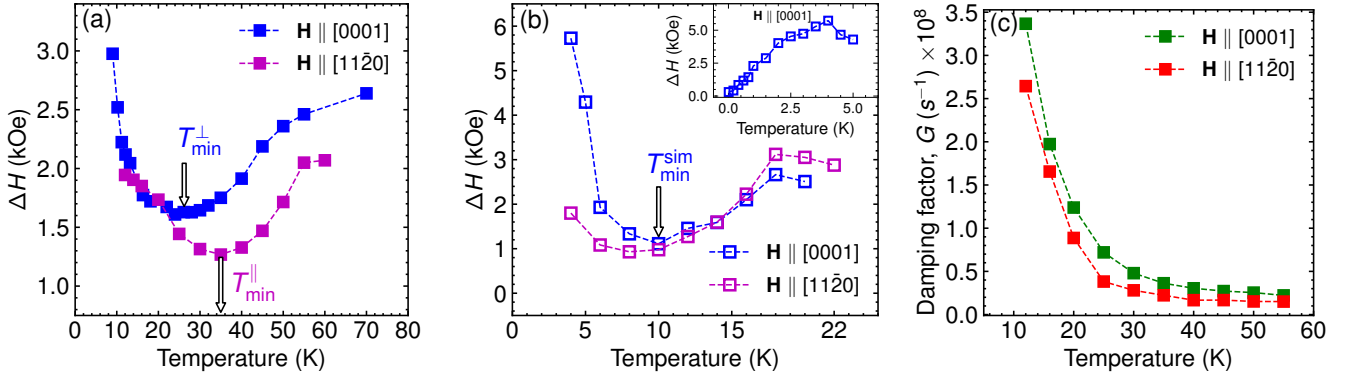


Figure 7. (Color online) (a) Measured temperature dependence of the linewidth ΔH for two magnetic field orientations: $\mathbf{H} \parallel [0001]$ (blue symbols) and $\mathbf{H} \parallel [11\bar{2}0]$ (magenta symbols). The temperatures at which ΔH attains its minimum values are marked as T_{\min}^{\perp} and T_{\min}^{\parallel} , respectively. (b) Simulated temperature dependence of the linewidth ΔH for the magnetic field orientation $\mathbf{H} \parallel [0001]$ (open blue symbols). The inset in (b) shows the computed results in a wider temperature range for $\mathbf{H} \parallel [0001]$. (c) Temperature dependence of damping factor, G for two magnetic field orientations: $\mathbf{H} \parallel [0001]$ (green symbols) and $\mathbf{H} \parallel [11\bar{2}0]$ (red symbols). Lines are guides for the eye.

temperatures, up to about 55 K, is attributed to enhanced homogeneous damping associated with the decreasing magnetization of individual clusters, as described by Eq.(10). These clusters contain Mn^{3+} ions that remain sufficiently strongly coupled to produce a detectable FMR signal at temperatures well above 12 K, the Curie temperature of the film determined from direct magnetization measurements.

The observed trend in $\Delta H(T)$ is typical for many ferromagnetic systems [77, 81–83]. The same trend is visible in Fig. 7 (b) which illustrates the temperature dependence of ΔH obtained from simulations. Similar to experimental observations a significant broadening of ΔH is noted at lower temperatures. As the temperature increases, ΔH narrows, reaching a minimum value of 1 kOe at approximately at 10 K denoted by T_{\min}^{sim} . Upon further temperature increase, ΔH slightly broadens again, reaching a maximum at 18 K. Although the obtained values differ from the experimental ones, they are comparable if presented in reduced temperature T/T_C .

IV. SUMMARY

In this study, we have thoroughly investigated the magnetic anisotropy and relaxation dynamics in percolating ferromagnetic semiconductor $Ga_{1-x}Mn_xN$ film with $x \sim 8\%$ using ferromagnetic resonance (FMR) and magnetometry. Our results confirm the ferromagnetic nature of the material, dominated by Mn^{3+} ions, which for this Mn dilution yields a clear ferromagnetic response below $T_C = 12$ K.

While the FMR signal is absent at low temperatures ($T < 9$ K) due to excessive line broadening that prevents detection, the signal persists up to 70 K, revealing the presence of non-percolating FM clusters (macrospins) above T_C . The temperature dependence of the signal intensity mirrors that of the magnetization up to 55 K, suggesting that the magnetic characteristics of the clusters remain relatively stable across this temperature range. Furthermore, the evolution of the FMR signal with temperature provides direct evidence of the progressive fragmentation of the percolating ferromagnetic network into isolated macrospins.

A crucial observation from our study is that while $(Ga,Mn)N$ exhibits percolative ferromagnetism, it retains essential features of conventional ferromagnetic materials, particularly in its resonance behavior. The dominance of uniaxial anisotropy with the easy axis perpendicular to the c -axis across the whole temperature range studied here confirms the dominant role of Mn^{3+} single ion magnetic anisotropy. Despite prior reports suggesting the possible influence of static Jahn-Teller distortions, our FMR results do not show evidence of such effects, implying a transition from a static to a dynamic Jahn-Teller regime at the temperatures studied here.

Our atomistic spin model simulations qualitatively reproduce the experimentally observed trends, providing further insights into the nature of ferromagnetic interactions in this dilute system. While the agreement between experiment and simulation is satisfactory, further refinements in modeling Mn-Mn interactions, especially in the presence of short-range disorder, are necessary for more accurate predictions. The combined use of SQUID

and FMR techniques allows us to bridge the gap between static and dynamic magnetic properties, illustrating the complex yet highly informative nature of percolating ferromagnetic semiconductors.

In summary, our study confirms that FMR serves as a powerful complementary technique to magnetometry for probing the magnetic behavior of percolating ferromagnetic systems like (Ga,Mn)N. The persistence of FMR signals above T_C highlights the role of non percolating ferromagnetic clusters. Our findings provide new insights into the interplay between magnetization dynamics, anisotropy, and percolation effects in (Ga,Mn)N, contributing to the broader understanding of percolating ferromagnetic systems and their potential relevance for spintronic applications, even well above T_C .

V. ACKNOWLEDGMENTS

The work is supported by the National Science Centre (Poland) through project OPUS 2018/31/B/ST3/03438.

A. MAGNETOMETRY DETAILS

The recorded signals from the (Ga,Mn)N films are weak, below 10^{-6} emu at remanence, and significantly smaller than the signals from the substrate at high magnetic fields [84]. The samples are measured both in perpendicular and in-plane orientations, i. e. with $\mathbf{H} \parallel \mathbf{c}$ or $\mathbf{H} \perp \mathbf{c}$, respectively.

The magnetothermal properties are examined in weak static magnetic fields using standard field-cooled (FC) and thermo-remanent magnetization (TRM) procedures. Special care is taken to ensure an extremely weak residual magnetic field (estimated to be approximately 0.15 Oe) during the TRM measurements. To achieve this condition, the entire system, including the sample, is de-gaussed at 300 K prior to the TRM measurements by applying an oscillating magnetic field gradually reduced to zero. Subsequently, the sample is field cooled from 300 to 2 K. We underline here that the near-zero field conditions at the base temperature, $T = 2$ K, are established by a soft quench of the MPMS's superconducting magnet. This procedure is carried out using the *magnet reset option* of the MPMS-XL system.

In this respect (Ga,Mn)N and other strongly dilute compounds in which randomly distributed magnetic species are coupled by a short range interaction constitute a class on their own, for which the correct methodology of T_C determination is yet to be firmly established. Earlier studies of criticality in (Ga,Mn)N showed that all the

traditional magnetometric approaches, such as the temperature dependence of: AC-susceptibility, the inverse of the static susceptibility, disappearance of the coercive field H_C , as well as of the thermoremanent magnetization give nearly the same values of the critical temperature [21, 22]. Some small discrepancies among these values are caused by a smeared character of the Curie transition in dilute systems, either due to the formation of magnetic clusters [85] or to the presence of a nonzero variance in the Mn distribution [21].

B. SIMULATION DETAILS

In this Appendix, we provide detailed descriptions of the numerical simulation methodology outlined in the main text, including the complete Hamiltonian, the equations of motion, and the parameter values used in the simulations. The experimental results are modeled in the frame of an atomistic spin model [46] supplemented with stochastic Landau-Lifshitz-Gilbert (sLLG) equation. We use a simulation box of about $25 \times 25 \times 5$ nm³ consisting of approximately 124820 wurtzite lattice cation sites on which the dynamics of 9860 randomly distributed Mn spins ($x = 7.9\%$) is simulated. In-plane periodic boundary conditions are implemented to model a large thin film. We follow the procedure presented in [36].

We use the following Hamiltonian:

$$\mathcal{H} = - \underbrace{\sum_{\langle i,j \rangle} J_{ij} \mathbf{S}_i \cdot \mathbf{S}_j}_{\text{Exchange}} - \frac{1}{4} K^{TR} \underbrace{\sum_i [S_{iz}^2 - (S_{ix}^2 + S_{iy}^2)]}_{\text{Trigonal}} - \frac{1}{2} K^{JT} \underbrace{\sum_i \sum_{j=A,B,C} (\mathbf{S}_i \cdot \mathbf{e}_j^{JT})^4}_{\text{Jahn-Teller}} \underbrace{- \mu_S \sum_i \mathbf{H} \cdot \mathbf{S}_i}_{\text{Zeeman}}, \quad (12)$$

which consists of the Zeeman energy, magnetocrystalline energy and ferromagnetic superexchange interaction between Mn ions. Here, \mathbf{S}_i describes the normalized local magnetic moment of Mn ion located at site i with magnitude $\mu_S = gS\mu_B$, where $g = 2$, $S = 2$ and μ_B is the Bohr magneton. The magnetocrystalline energy is composed of trigonal and Jahn-Teller anisotropies [36, 47], with $\mathbf{e}_A^{JT} = [\sqrt{\frac{2}{3}}, 0, \sqrt{\frac{1}{3}}]$, $\mathbf{e}_B^{JT} = [-\sqrt{\frac{1}{6}}, -\sqrt{\frac{1}{2}}, \sqrt{\frac{1}{3}}]$, $\mathbf{e}_C^{JT} = [-\sqrt{\frac{1}{6}}, \sqrt{\frac{1}{2}}, \sqrt{\frac{1}{3}}]$. Finally, the Mn ions are coupled through a ferromagnetic superexchange interaction of Heisenberg form. We take into account interactions up to the 14th nearest neighbors approximated by

$J_{ij} = J_0 \exp(R_{ij}/b)$, with R_{ij} being the distance between ions \mathbf{S}_i and \mathbf{S}_j .

To calculate the magnetization as a function of external magnetic field $\mathbf{M}(H)$ at a nonzero temperature we initialize the system at a high magnetic field in a completely random spin state. The spin system evolves according to the sLLG equation [36, 47].

$$\frac{\partial \mathbf{S}_i}{\partial t} = -\frac{\gamma}{1 + \alpha_G^2} [\mathbf{S}_i \times \mathbf{H}_{\text{eff}}^{i,\text{tot}} + \alpha_G \mathbf{S}_i \times (\mathbf{S}_i \times \mathbf{H}_{\text{eff}}^{i,\text{tot}})], \quad (13)$$

where γ and α_G are the gyromagnetic ratio and the precession damping term, respectively. The total effective magnetic field acting on i -th spin $\mathbf{H}_{\text{eff}}^{i,\text{tot}}$ consists of the Zeeman, exchange and anisotropy field $\mathbf{H}_{\text{eff}}^i = -(1/\mu_S) \partial \mathcal{H} / \partial \mathbf{S}_i$ and the thermal field \mathbf{H}_{th}^i ([46, 86, 87]). Here \mathbf{H}_{th}^i represents thermal fluctuations (a nonzero temperature) in the system and is modeled as random magnetic field generated in every sLLG iteration according to:

$$\mathbf{H}_{th}^i = \Gamma(t) \sqrt{\frac{2\alpha_G k_B T}{\gamma \mu_S \Delta t}}, \quad (14)$$

where $\Gamma(t)$ is a 3D Gaussian random vector with a standard deviation of 1 and mean of zero, and $\Delta t = 5 \cdot 10^{-6}$ ns is the integration time step. The simulation is advanced over time and \mathbf{M} is computed after the system has reached a steady state. This steady-state spin configuration then serves as the initial condition for the subsequent simulation step with a slightly reduced \mathbf{H} . The iterative reduction of \mathbf{H} and corresponding steady-state measurements enable us to construct a detailed $\mathbf{M}(H)$ curve.

All the numerical results presented in this study are obtained with $J_{nn} = 4$ meV, $b = 1.1$ Å, $K^{TR} = 0.05$ meV/atom, $K^{JT} = 0.75$ meV/atom, and $\alpha_G = 0.1$.

To calculate the temperature dependence of M we initialize at $T = 0.1$ K the same numerical box with all the spins aligned in the easy plane, that is perpendicular to c -axis. To reproduce the TRM data, a very weak field $H = 1$ Oe is set along the direction of the spins. However, for this simulation, we use a Monte Carlo approach to thermally equilibrate the spins. The system is iterated with a sufficient number of Monte Carlo steps per site (MCS/site) [60], where for each MCS, a trial spin orientation change is proposed, and the change in energy ΔE is calculated. The trial move is accepted or rejected based on the Metropolis criterion. The system is considered to have reached equilibrium once the magnetization stabilizes, showing no significant fluctuations. After determining the resulting M , the simulation proceeds with the temperature increment, at which the previous spin

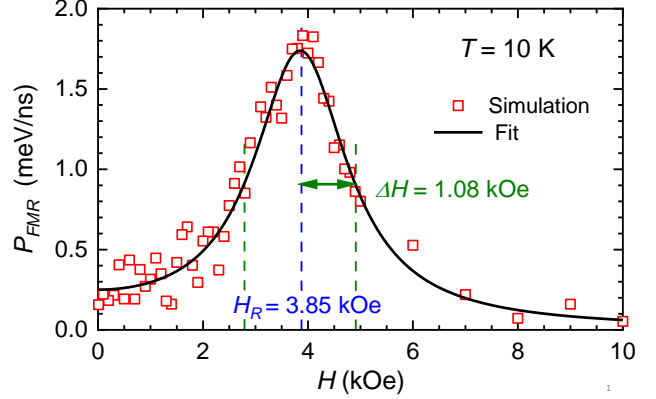


Figure 8. (Color online) Open squares show an example of the simulated ferromagnetic resonance spectrum, obtained within the same framework described here. The solid line represents a fit using a collision-broadened Lorentzian line-shape function (Eq. 15), yielding the resonance field H_R and linewidth ΔH for this particular simulation.

configuration is taken as the starting one. The procedure is repeated until the full $M(T)$ curve is established [61].

To model FMR, we add a sinusoidal AC magnetic field (\mathbf{h}_{AC}) with a frequency $\nu = 9.54$ GHz to the external field \mathbf{H} ensuring that $\mathbf{h}_{AC} \perp \mathbf{H}$ [62]. First, we start with a completely random spin orientation and a very high magnetic field $H = 60$ kOe. The system is allowed to evolve within the sLLG frame until it reaches a steady state, at which we calculate the microwave power absorbed during FMR: $P_{\text{FMR}} = -\frac{\mu_S}{Nt_0} \sum_i \int_t^{t+t_0} \mathbf{S}_i \frac{\partial \mathbf{h}_{AC}(t)}{\partial t} dt$, where N is the number of Mn ions and t_0 is simulation time [62]. Next, this steady-state spin configuration is used as the initial condition for the next simulation step, in which the external field \mathbf{H} is slightly reduced. This process is repeated iteratively, until \mathbf{H} reaches zero. Exemplary $P_{\text{FMR}}(H)$ simulation data are depicted in Fig. 8 by open symbols.

The resonance field H_R and the line-width ΔH of the simulated FMR are determined at the given T by fitting the collision-broadened Lorentzian line-shape function $f(H)$ [88]:

$$f(H) = \frac{A}{\pi} \left[\frac{\Delta H}{(H - H_R)^2 + \Delta H^2} + \frac{\Delta H}{(H + H_R)^2 + \Delta H^2} \right] \quad (15)$$

to the modeled $P_{\text{FMR}}(H)$. A result of such a fit is represented by solid line in Fig. 8. The entire process is repeated for temperatures ranging from 2 to 22 K.

Technically, in the sLLG simulations, the code is parallelized by dividing the simulation region into sections,

with each processor handling a specific part of the system. Computations are accelerated using graphics processing units (GPUs), and Euler's method is employed as the integration scheme. Since a higher temperature introduces more disturbance in the system, the initialization and averaging steps of the sLLG simulations are adjusted as specified in table I.

Table I. Parameters of atomistic spin model simulations.

Temperature (K)	Number of initialization steps	Number of averaging steps
0.01 to 0.40	1×10^7	1×10^7
0.60	1×10^7	3×10^7
0.80 to 1.00	1×10^7	4×10^7
1.50	1×10^7	6×10^7
2.00	2×10^7	5×10^7
2.50	2×10^7	6×10^7
3.00 to 3.50	2×10^7	8×10^7
4 to 22	6×10^7	6×10^8

- [1] H. Ohno, Making nonmagnetic semiconductors ferromagnetic, *Science* **281**, 951 (1998).
- [2] T. Dietl, H. Ohno, F. Matsukura, J. Cibert, and D. Ferrand, Zener model description of ferromagnetism in zinc-blende magnetic semiconductors, *Science* **287**, 1019 (2000).
- [3] S. Pearton, C. Abernathy, D. Norton, A. Hebard, Y. Park, L. Boatner, and J. Budai, Advances in wide bandgap materials for semiconductor spintronics, *Mater. Sci. Eng. R.* **40**, 137 (2003).
- [4] T. Dietl, H. Ohno, and F. Matsukura, Hole-mediated ferromagnetism in tetrahedrally coordinated semiconductors, *Phys. Rev. B* **63**, 195205 (2001).
- [5] T. Dietl, K. Sato, T. Fukushima, A. Bonanni, M. Jamet, A. Barski, S. Kuroda, M. Tanaka, P. N. Hai, and H. Katayama-Yoshida, Spinodal nanodecomposition in semiconductors doped with transition metals, *Rev. Mod. Phys.* **87**, 1311 (2015).
- [6] M. Iwinska, M. Zajac, B. Lucznik, M. Fijalkowski, M. Amilusik, T. Sochacki, E. Litwin-Staszewska, R. Piotrzkowski, I. Grzegory, and M. Bockowski, Iron and manganese as dopants used in the crystallization of highly resistive HVPE-GaN on native seeds, *Jpn. J. Appl. Phys.* **58**, SC1047 (2019).
- [7] A. Bonanni, M. Sawicki, T. Devillers, W. Stefanowicz, B. Faina, Tian Li, T. E. Winkler, D. Sztenkiel, A. Navarro-Quezada, M. Rovezzi, R. Jakieła, A. Grois, M. Wegscheider, W. Jantsch, J. Suffczyński, F. D'Acapito, A. Meingast, G. Kothleitner, and T. Dietl, Experimental probing of exchange interactions between localized spins in the dilute magnetic insulator (Ga,Mn)N, *Phys. Rev. B* **84**, 035206 (2011).
- [8] T. Yamamoto, H. Sazawa, N. Nishikawa, M. Kiuchi, T. Ide, M. Shimizu, T. Inoue, and M. Hata, Reduction in buffer leakage current with Mn-doped GaN buffer layer grown by metal organic chemical vapor deposition, *Jpn. J. Appl. Phys.* **52**, 08JN12 (2013).
- [9] L. Janicki, G. Kunert, M. Sawicki, E. Piskorska-Hommel, K. Gas, R. Jakieła, D. Hommel, and R. Kudrawiec, Fermi level and bands offsets determination in insulating (Ga,Mn)N/GaN structures, *Sci. Rep.* **7**, 41877 (2017).
- [10] J. Kreissl, W. Ulrici, M. El-Metoui, A. -M. Vasson, A. Vasson, and A. Gavaix, Neutral manganese acceptor in GaP: An electron-paramagnetic-resonance study, *Phys. Rev. B* **54**, 10508 (1996).
- [11] T. Dietl, Origin and control of ferromagnetism in dilute magnetic semiconductors and oxides (invited), *J. Appl. Phys.* **103**, 07D111 (2008).
- [12] J. Blinowski, P. Kacmar, and J. A. Majewski, Ferromagnetic superexchange in Cr-based diluted magnetic semiconductors, *Phys. Rev. B* **53**, 9524 (1996).
- [13] M. Sawicki, T. Devillers, S. Gałęski, C. Simserides, S. Dobkowska, B. Faina, A. Grois, A. Navarro-Quezada, K. N. Trohidou, J. A. Majewski, T. Dietl, and A. Bonanni, Origin of low-temperature magnetic ordering in $\text{Ga}_{1-x}\text{Mn}_x\text{N}$, *Phys. Rev. B* **85**, 205204 (2012).
- [14] C. Śliwa and T. Dietl, Tight-binding theory of spin-spin interactions, Curie temperatures, and quantum hall effects in topological (Hg,Cr)Te in comparison to nontopological (Zn,Cr)Te and (Ga,Mn)N, *Phys. Rev. B* **110**, 165201 (2024).

- [15] E. Piskorska-Hommel and K. Gas, (Ga,Mn)N—Epitaxial growth, structural, and magnetic characterization—Tutorial, *J. Appl. Phys.* **135**, 071101 (2024).
- [16] I. Ya. Korenblit, E. F. Shender, and B. I. Shklovsky, Percolation approach to the phase transition in the very dilute ferromagnetic alloys, *Phys. Lett. A* **46**, 275 (1973).
- [17] L. Bergqvist, O. Eriksson, J. Kudrnovský, V. Drchal, P. Korzhavyi, and I. Turek, Magnetic percolation in diluted magnetic semiconductors, *Phys. Rev. Lett.* **93**, 137202 (2004).
- [18] A. Bonanni, T. Dietl, and H. Ohno, Dilute magnetic materials, in *Handbook on Magnetism and Magnetic Materials*, edited by J. M. D. Coey and S. S. P. Parkin (Springer, Berlin, 2021).
- [19] E. Sarigiannidou, F. Wilhelm, E. Monroy, R. M. Galera, E. Bellet-Amalric, A. Rogalev, J. Goulon, J. Cibert, and H. Mariette, Intrinsic ferromagnetism in wurtzite (Ga,Mn)N semiconductor, *Phys. Rev. B* **74**, 041306(R) (2006).
- [20] G. Kunert, S. Dobkowska, Tian Li, H. Reuther, C. Kruse, S. Figge, R. Jakiela, A. Bonanni, J. Grenzer, W. Stefanowicz, J. von Borany, M. Sawicki, T. Dietl, and D. Hommel, $\text{Ga}_{1-x}\text{Mn}_x\text{N}$ epitaxial films with high magnetization, *Appl. Phys. Lett.* **101**, 022413 (2012).
- [21] S. Stefanowicz, G. Kunert, C. Simserides, J. A. Majewski, W. Stefanowicz, C. Kruse, S. Figge, Tian Li, R. Jakiela, K. N. Trohidou, A. Bonanni, D. Hommel, M. Sawicki, and T. Dietl, Phase diagram and critical behavior of a random ferromagnet $\text{Ga}_{1-x}\text{Mn}_x\text{N}$, *Phys. Rev. B* **88**, 081201(R) (2013).
- [22] K. Gas, J. Z. Domagala, R. Jakiela, G. Kunert, P. Dluzewski, E. Piskorska-Hommel, W. Paszkowicz, D. Sztenkiel, M. J. Winiarski, D. Kowalska, R. Szukiewicz, T. Baraniecki, A. Miszcuk, D. Hommel, and M. Sawicki, Impact of substrate temperature on magnetic properties of plasma-assisted molecular beam epitaxy grown (Ga,Mn)N, *J. Alloys Compd.* **747**, 946 (2018).
- [23] M. Sawicki, Magnetic properties of (Ga,Mn)As, *J. Magn. Magn. Mater.* **300**, 1 (2006).
- [24] T. Jungwirth, J. Mašek, K. Y. Wang, K. W. Edmonds, M. Sawicki, M. Polini, J. Sinova, A. H. MacDonald, R. P. Campion, L. X. Zhao, N. R. S. Farley, T. K. Johal, G. van der Laan, C. T. Foxon, and B. L. Gallagher, Low-temperature magnetization of (Ga,Mn)As semiconductors, *Phys. Rev. B* **73**, 165205 (2005).
- [25] T. Jungwirth, K. Y. Wang, J. Mašek, K. W. Edmonds, J. König, J. Sinova, M. Polini, N. A. Goncharuk, A. H. MacDonald, M. Sawicki, R. P. Campion, L. X. Zhao, C. T. Foxon, and B. L. Gallagher, Prospects for high temperature ferromagnetism in (Ga,Mn)As semiconductors, *Phys. Rev. B* **72**, 165204 (2005).
- [26] J. Sadowski, S. Kret, A. Šiušys, T. Wojciechowski, K. Gas, M. F. Islam, C. M. Canali, and M. Sawicki, Wurtzite (Ga,Mn)As nanowire shells with ferromagnetic properties, *Nanoscale* **9**, 2129 (2017).
- [27] L. Gluba, O. Yastrubchak, J. Z. Domagala, R. Jakiela, T. Andreadczyk, J. Žuk, T. Wosinski, J. Sadowski, and M. Sawicki, Band structure evolution and the origin of magnetism in (Ga,Mn)As: From paramagnetic through superparamagnetic to ferromagnetic phase, *Phys. Rev. B* **97**, 115201 (2018).
- [28] M. Sawicki, D. Chiba, A. Korbecka, Y. Nishitani, J. A. Majewski, F. Matsukura, T. Dietl, and H. Ohno, Experimental probing of the interplay between ferromagnetism and localization in (Ga,Mn)As, *Nat. Phys.* **6**, 22 (2010).
- [29] O. Proselkov, D. Sztenkiel, W. Stefanowicz, M. Aleszkiewicz, J. Sadowski, T. Dietl, and M. Sawicki, Thickness dependent magnetic properties of (Ga,Mn)As ultrathin films, *Appl. Phys. Lett.* **100**, 262405 (2012).
- [30] L. Chen, F. Matsukura, and H. Ohno, Electric-field modulation of damping constant in a ferromagnetic semiconductor (Ga,Mn)As, *Phys. Rev. Lett.* **115**, 057204 (2015).
- [31] T. Dietl, Interplay between carrier localization and magnetism in diluted magnetic and ferromagnetic semiconductors, *J. Phys. Soc. Jpn.* **77**, 031005 (2008).
- [32] M. A. Mayer, P. R. Stone, N. Miller, H. M. Smith, O. D. Dubon, E. E. Haller, K. M. Yu, W. Walukiewicz, X. Liu, and J. K. Furdyna, Electronic structure of $\text{Ga}_{1-x}\text{Mn}_x\text{As}$ analyzed according to hole-concentration-dependent measurements, *Phys. Rev. B* **81**, 045205 (2010).
- [33] A. Richardella, P. Roushan, S. Mack, B. Zhou, D. A. Huse, D. D. Awschalom, and A. Yazdani, Visualizing critical correlations near the metal-insulator transition in $\text{Ga}_{1-x}\text{Mn}_x\text{As}$, *Science* **327**, 665 (2010).
- [34] J. Gosk, M. Zajac, A. Wolos, M. Kaminska, A. Twardowski, I. Grzegory, M. Bockowski, and S. Porowski, Magnetic anisotropy of bulk GaN:Mn single crystals codoped with Mg acceptors, *Phys. Rev. B* **71**, 094432 (2005).
- [35] K. Das, N. G. Szwacki, R. Hayn, and D. Sztenkiel, Jahn-Teller effect and pair anisotropy in wurtzite $\text{Ga}_{1-x}\text{Mn}_x\text{N}$ **10.48550/ARXIV.2410.22035** (2024).
- [36] D. Sztenkiel, K. Gas, N. G. Szwacki, M. Foltyn, C. Śliwa, T. Wojciechowski, J. Domagala, D. Hommel, M. Sawicki, and T. Dietl, Electric field manipulation of magnetization in an insulating dilute ferromagnet through piezoelectromagnetic coupling, *Commun. Mater.* **6**, 16 (2025).
- [37] T. Graf, M. Gjukic, M. S. Brandt, M. Stutzmann, and O. Ambacher, The $\text{Mn}^{3+/2+}$ acceptor level in group III nitrides, *Appl. Phys. Lett.* **81**, 5159 (2002).
- [38] A. Wolos, M. Palczewska, M. Zajac, J. Gosk, M. Kaminska, A. Twardowski, M. Bockowski, I. Grzegory, and S. Porowski, Optical and magnetic properties of Mn in bulk GaN, *Phys. Rev. B* **69**, 115210 (2004).
- [39] A. Wolos, A. Wysmolek, M. Kaminska, A. Twardowski, M. Bockowski, I. Grzegory, S. Porowski, and M. Potemski, Neutral Mn acceptor in bulk GaN in high magnetic fields, *Phys. Rev. B* **70**, 245202 (2004).
- [40] J. T. Vallin, G. A. Slack, S. Roberts, and A. E. Hughes, Infrared absorption in some II-VI compounds doped with Cr, *Phys. Rev. B* **2**, 4313 (1970).
- [41] J. T. Vallin and G. D. Watkins, EPR of Cr^{2+} in II-VI lattices, *Phys. Rev. B* **9**, 2051 (1974).

- [42] M. Herbich, W. Mac, A. Twardowski, K. Ando, Y. Shapira, and M. Demianiuk, Magnetization and exciton spectroscopy of the diluted magnetic semiconductor $\text{Cd}_{1-x}\text{Cr}_x\text{S}$, *Phys. Rev. B* **58**, 1912 (1998).
- [43] W. Stefanowicz, D. Sztenkiel, B. Faina, A. Grois, M. Rovezzi, T. Devillers, F. d'Acapito, A. Navarro-Quezada, Tian Li, R. Jakieła, M. Sawicki, T. Dietl, and A. Bonanni, Structural and paramagnetic properties of dilute $\text{Ga}_{1-x}\text{Mn}_x\text{N}$, *Phys. Rev. B* **81**, 235210 (2010).
- [44] D. Sztenkiel, M. Foltyn, G. P. Mazur, R. Adhikari, K. Kosiel, K. Gas, M. Zgirski, R. Kruszka, R. Jakieła, Tian Li, A. Piotrowska, A. Bonanni, M. Sawicki, and T. Dietl, Stretching magnetism with an electric field in a nitride semiconductor, *Nat. Commun* **7**, 13232 (2016).
- [45] D. Sztenkiel, K. Gas, J. Domagala, D. Hommel, and M. Sawicki, Crystal field model simulations of magnetic response of pairs, triplets and quartets of Mn^{3+} ions in GaN, *New. J. Phys.* **22**, 123016 (2020).
- [46] R. F. L. Evans, W. J. Fan, P. Chureemart, T. A. Ostler, M. O. A. Ellis, and R. W. Chantrell, Atomistic spin model simulations of magnetic nanomaterials, *J. Phys.: Condens. Matt.* **26**, 103202 (2014).
- [47] Y. K. Edathumkandy and D. Sztenkiel, Comparative study of magnetic properties of Mn^{3+} magnetic clusters in GaN using classical and quantum mechanical approach, *J. Magn. Magn. Mater.* **562**, 169738 (2022).
- [48] H. Nakayama, M. Althammer, Y.-T. Chen, K. Uchida, Y. Kajiwara, D. Kikuchi, T. Ohtani, S. Geprägs, M. Opel, S. Takahashi, R. Gross, G. E. W. Bauer, S. T. B. Goennenwein, and E. Saitoh, Spin Hall magnetoresistance induced by a nonequilibrium proximity effect, *Phys. Rev. Lett.* **110**, 206601 (2013).
- [49] J. A. Mendoza-Rodarte, K. Gas, M. Herrera-Zaldívar, D. Hommel, M. Sawicki, and M. H. D. Guimarães, Spin Hall magnetoresistance in Pt/(Ga,Mn)N devices, *Appl. Phys. Lett.* **125**, 152404 (2024).
- [50] M. Farle, Ferromagnetic resonance of ultrathin metallic layers, *Rep. Prog. Phys.* **61**, 755 (1998).
- [51] X. Liu, Y. Sasaki, and J. K. Furdyna, Ferromagnetic resonance in $\text{Ga}_{1-x}\text{Mn}_x\text{As}$: Effects of magnetic anisotropy, *Phys. Rev. B* **67**, 205204 (2003).
- [52] Y. Sasaki, X. Liu, J. K. Furdyna, M. Palczewska, J. Szczytko, and A. Twardowski, Ferromagnetic resonance in GaMnAs, *J. Appl. Phys.* **91**, 7484 (2002).
- [53] Y. Y. Zhou, X. Liu, J. K. Furdyna, M. A. Scarpulla, and O. D. Dubon, Ferromagnetic resonance investigation of magnetic anisotropy in $\text{Ga}_{1-x}\text{Mn}_x\text{As}$ synthesized by ion implantation and pulsed laser melting, *Phys. Rev. B* **80**, 224403 (2009).
- [54] C. Bihler, M. Kraus, H. Huebl, M. S. Brandt, S. T. B. Goennenwein, M. Opel, M. A. Scarpulla, P. R. Stone, R. Farshchi, and O. D. Dubon, Magnetocrystalline anisotropy and magnetization reversal in $\text{Ga}_{1-x}\text{Mn}_x\text{P}$ synthesized by ion implantation and pulsed-laser melting, *Phys. Rev. B* **75**, 214419 (2007).
- [55] K. G. et al., Magnetic anisotropy of paramagnetic Mn^{3+} in GaN (2025), manuscript in preparation.
- [56] M. Sawicki, W. Stefanowicz, and A. Ney, Sensitive SQUID magnetometry for studying nanomagnetism, *Semicon. Sci. Technol.* **26**, 064006 (2011).
- [57] L. M. C. Pereira, J. P. Araújo, M. J. V. Bael, K. Temst, and A. Vantomme, Practical limits for detection of ferromagnetism using highly sensitive magnetometry techniques, *J. Phys. D: Appl. Phys.* **44**, 215001 (2011).
- [58] K. Gas and M. Sawicki, In situ compensation method for high-precision and high-sensitivity integral magnetometry, *Meas. Sci. Technol.* **30**, 085003 (2019).
- [59] K. Gas and M. Sawicki, A simplified method of the assessment of magnetic anisotropy of commonly used sapphire substrates in SQUID magnetometers, *Materials* **15**, 10.3390/ma15238532 (2022).
- [60] Y. Zhang, B. Wang, Y. Guo, Q. Li, and J. Wang, A universal framework for metropolis Monte Carlo simulation of magnetic Curie temperature, *Comput. Mater. Sci.* **197**, 110638 (2021).
- [61] V. V. Prudnikov, P. V. Prudnikov, and D. E. Romanovskiy, Monte Carlo simulation of magnetic multilayered structures with giant magnetoresistance effects, *J. Phys. Conf. Ser.* **681**, 012016 (2016).
- [62] K. D. Usadel, Temperature-dependent dynamical behavior of nanoparticles as probed by ferromagnetic resonance using Landau-Lifshitz-Gilbert dynamics in a classical spin model, *Phys. Rev. B* **73**, 212405 (2006).
- [63] K. Fabian, V. P. Shcherbakov, and S. A. McEnroe, Measuring the curie temperature, *Geochemistry, Geophysics, Geosystems* **14**, 947 (2013).
- [64] M. Wang, K. W. Edmonds, B. L. Gallagher, A. W. Rushforth, O. Makarovsky, A. Patané, R. P. Campion, C. T. Foxon, V. Novak, and T. Jungwirth, High Curie temperatures at low compensation in the ferromagnetic semiconductor (Ga,Mn)As, *Phys. Rev. B* **87**, 121301 (2013).
- [65] K. Gas, A. Królicka, K. Dybko, P. Nowicki, Z. Khosravizadeh, T. Story, and M. Sawicki, Magnetic constitution of topologically trivial thermoelectric PbTe:Cr, *J. Magn. Magn. Mater.* **537**, 168154 (2021).
- [66] K. Kalbarczyk, K. Dybko, K. Gas, D. Sztenkiel, M. Foltyn, M. Majewicz, P. Nowicki, E. Łusakowska, D. Hommel, and M. Sawicki, Electrical characteristics of vertical-geometry Schottky junction to magnetic insulator (Ga,Mn)N heteroepitaxially grown on sapphire, *Journal of Alloys and Compounds* **804**, 415 (2019).
- [67] D. Sztenkiel, Spin orbital reorientation transitions induced by magnetic field, *Journal of Magnetism and Magnetic Materials* **572**, 170644 (2023).
- [68] P. R. Stone, M. A. Scarpulla, R. Farshchi, I. D. Sharp, E. E. Haller, O. D. Dubon, K. M. Yu, J. W. Beeman, E. Arenholz, J. D. Denlinger, and H. Ohldag, Mn L_{3,2} x-ray absorption and magnetic circular dichroism in ferromagnetic $\text{Ga}_{1-x}\text{Mn}_x\text{P}$, *Appl. Phys. Lett.* **89**, 012504 (2006).
- [69] R. N. Bhatt, Magnetic properties of doped semiconductors, *Phys. Scr.* **T14**, 7 (1986).
- [70] J. R. Anderson, M. Górska, L. J. Azevedo, and E. L. Venturini, Magnetization of $\text{Hg}_{1-x}\text{Mn}_x\text{Te}$, *Phys. Rev. B* **33**, 4706 (1986).

- [71] R. N. Bhatt and P. A. Lee, Scaling studies of highly disordered spin-1/2 antiferromagnetic systems, *Phys. Rev. Lett.* **48**, 344 (1982).
- [72] T. Dietl, Localization and magnetic interactions in semi-magnetic semiconductors at low temperatures, *Jpn. J. Appl. Phys.* **26**, 1907 (1987).
- [73] M. Sawicki, E. Guziewicz, M. I. Łukasiewicz, O. Proskov, I. A. Kowalik, W. Lisowski, P. Dluzewski, A. Wittlin, M. Jaworski, A. Wolska, W. Paszkowicz, R. Jakiel, B. S. Witkowski, L. Wachnicki, M. T. Klepka, F. J. Luque, D. Arvanitis, J. W. Sobczak, M. Krawczyk, A. Jablonski, W. Stefanowicz, D. Sztenkiel, M. Godlewski, and T. Dietl, Homogeneous and heterogeneous magnetism in (Zn,Co)O: From a random antiferromagnet to a dipolar superferromagnet by changing the growth temperature, *Phys. Rev. B* **88**, 085204 (2013).
- [74] A. Wolos, A. Wysmolek, M. Kaminska, A. Twardowski, M. Bockowski, I. Grzegory, S. Porowski, and M. Potemski, Neutral Mn acceptor in bulk GaN in high magnetic fields, *Phys. Rev. B* **70**, 245202 (2004).
- [75] J. Smit and H. G. Beljers, *Philips Res. Rep.* **10**, 113 (1955).
- [76] H. Suhl, Ferromagnetic resonance in nickel ferrite between one and two kilomegacycles, *Phys. Rev.* **97**, 555 (1955).
- [77] W. Platow, A. N. Anisimov, G. L. Dunifer, M. Farle, and K. Baberschke, Correlations between ferromagnetic-resonance linewidths and sample quality in the study of metallic ultrathin films, *Phys. Rev. B* **58**, 5611 (1998).
- [78] C. Chappert, K. L. Dang, P. Beauvillain, H. Hurdequin, and D. Renard, Ferromagnetic resonance studies of very thin cobalt films on a gold substrate, *Phys. Rev. B* **34**, 3192 (1986).
- [79] J. Sinova, T. Jungwirth, X. Liu, Y. Sasaki, J. K. Furdyna, W. A. Atkinson, and A. H. MacDonald, Magnetization relaxation in (Ga,Mn)As ferromagnetic semiconductors, *Phys. Rev. B* **69**, 085209 (2004).
- [80] Y. Matsuda, A. Oiwa, K. Tanaka, and H. Munekata, Ferromagnetic resonance study of magnetization relaxation in GaMnAs, *Physica B* **376-377**, 668 (2006), proceedings of the 23rd International Conference on Defects in Semiconductors.
- [81] Y. Li, M. Farle, and K. Baberschke, Critical spin fluctuations and curie temperatures of ultrathin Ni(111)/W(110): A magnetic-resonance study in ultrahigh vacuum, *Phys. Rev. B* **41**, 9596 (1990).
- [82] J. Kötzler and H. von Philipsborn, Critical speeding-up of spin-relaxation in CdCr₂Se₄, *Phys. Rev. Lett.* **40**, 790 (1978).
- [83] F. Spörel and E. Biller, Electron spin resonance in nickel near T_c , *Solid State Commun.* **17**, 833 (1975).
- [84] K. Gas, G. Kunert, P. Dluzewski, R. Jakiel, D. Hommel, and M. Sawicki, Improved-sensitivity integral SQUID magnetometry of (Ga,Mn)N thin films in proximity to Mg-doped GaN, *J. Alloys Compd* **868**, 159119 (2021).
- [85] R. B. Griffiths, Nonanalytic behavior above the critical point in a random Ising ferromagnet, *Phys. Rev. Lett.* **23**, 17 (1969).
- [86] B. Skubic, J. Hellsvik, L. Nordström, and O. Eriksson, A method for atomistic spin dynamics simulations: implementation and examples, *J. Phys.: Condens. Matt.* **20**, 315203 (2008).
- [87] R. F. L. Evans, U. Atxitia, and R. W. Chantrell, Quantitative simulation of temperature-dependent magnetization dynamics and equilibrium properties of elemental ferromagnets, *Phys. Rev. B* **91**, 144425 (2015).
- [88] J. H. Van Vleck and V. F. Weisskopf, On the shape of collision-broadened lines, *Rev. Mod. Phys.* **17**, 227 (1945).